# Asteroid Fragmentation Approaches for Modeling Atmospheric Energy Deposition

Paul J. Register, Donovan L. Mathias, Lorien F. Wheeler

## Abstract

During asteroid entry, energy is deposited in the atmosphere through thermal ablation and momentum-loss due to aerodynamic drag. Analytic models of asteroid entry and breakup physics are used to compute the energy deposition, which can then be compared against measured light curves and used to estimate ground damage due to airburst events. This work assesses and compares energy deposition results from four existing approaches to asteroid breakup modeling, and presents a new model that combines key elements of those approaches. The existing approaches considered include a liquid drop or "pancake" model where the object is treated as a single deforming body, and a set of discrete fragment models where the object breaks progressively into individual fragments. The new model incorporates both independent fragments and aggregate debris clouds to represent a broader range of fragmentation behaviors and reproduce more detailed light curve features. All five models are used to estimate the energy deposition rate versus altitude for the Chelyabinsk meteor impact, and results are compared with an observationally derived energy deposition curve. Comparisons show that four of the five approaches are able to match the overall observed energy deposition profile, but the features of the combined model are needed to better replicate both the primary and secondary peaks of the Chelyabinsk curve.

## 1. Introduction

As an asteroid descends through Earth's atmosphere, drag forces convert portions of its kinetic energy into light, heat, and pressure. The rate of this energy conversion is referred to as energy deposition and is often used to estimate potential ground damage due to blast waves or thermal radiation in asteroid impact risk assessments [1, 2, 3]. A notable challenge in developing and validating energy deposition models for risk assessment is the lack of observational evidence, particularly on the scale of objects large enough to present a threat to the population. However, observed light curves from smaller objects can serve as a basis for comparing and guiding energy deposition models. To accomplish this, the models are used to match observed light curves and, once a desired match is obtained, inference about the initial object and its breakup characteristics can be made based on the modeling approaches and parameters employed. Several existing studies [4, 5, 6] provide examples of such an approach.

Existing asteroid fragmentation models tend to follow either a liquid drop/pancake approach or a discrete fragment approach [7, 8]. In the liquid drop models [9, 10], the bolide remains intact until it meets a specified flight condition, at which point it is permitted to deform and spread into a "pancake" shape. This broadening shape presents an increasing frontal area to the flow, which

increases both the aerodynamic drag and mass ablation. Discrete fragment models [5, 6, 11], on the other hand, treat the breakup as a successive series of fragmentation events that split the body into individual pieces. Hybrid models that combine discrete fragmentation and pancaking behaviors have been discussed to a limited extent in previous literature, but specific models have not been published. For example, Artemieva [8, 12] discussed the notion of a "hybrid" model in the context of a computational simulation of discrete elements grouped to mimic a cloud, and Popova [13] has shown results suggesting a hybrid energy deposition approach but does not present the details of a particular model.

This paper compares energy deposition curves from one liquid drop model and three discrete fragment models, and presents a new combination model developed to incorporate advantageous features of both approaches. The Chelyabinsk event provides a basis for comparing all five models. Specifically, the fragmentation parameters of each model are varied to reproduce the energy deposition profile derived from the light curve of Brown [14]. The results are used to evaluate the advantages and limitations of the various approaches, and to suggest how energy deposition modeling can represent key entry events more generally. Due to the large uncertainties in the modeling parameters, the study concludes with a stochastic assessment using the newly developed combination model to examine sensitivity to the fragmentation assumptions and the range of energy deposition results they produce.

## 2. Model Descriptions

The following sections give an overview of the five fragmentation models implemented to compute atmospheric energy deposition in this work. The models presented are: a continuous fragmentation pancake model; three discrete fragmentation models with collective wake, non-collective wake, and independent wake treatments; and a combination model incorporating both continuous and discrete fragmentation components.

The flight physics and breakup assumptions common to all the models are presented first, followed by specific descriptions of the fragmentation approaches for each model. The primary difference among the existing models is how they treat the fragment interaction and wake behavior following breakup. From an energy deposition perspective, these differences manifest through differences in the projected frontal area, or drag area, compared to the system's mass. This ratio, described by the ballistic coefficient, measures how effectively the atmosphere slows the meteoroid. The drag area also impacts how much the air heats the meteoroid and ties directly to the mass ablation. For all of the current models, drag and ablation are the sources of energy deposited in the atmosphere. Finally, the atmospheric energy deposition computed from the flight and fragmentation is defined.

## *2.1 Flight Physics*

In all of the models considered, the standard equations for meteor physics [15] are integrated to determine the state of the bolide and its fragmentation components throughout their entry trajectory. Time derivatives of velocity $v$ (Eq. 1), flight path angle $\theta$ (Eq. 2), and mass $m$ (Eq. 3) are computed every time step. Instead of specifying an explicit time step, however, a constant altitude increment, $\Delta h$, is specified and a corresponding time step is calculated based on the instantaneous velocity and flight path angle (Eq. 4).

$$\frac{dv}{dt} = -\frac{\frac{1}{2}C_d A \rho_A v^2}{m} - g\sin\theta \tag{1}$$

$$\frac{d\theta}{dt} = \left(\frac{v}{R_E + h} - \frac{g}{v}\right)\cos\theta \tag{2}$$

$$\frac{dm}{dt} = -\frac{\frac{1}{2}\rho_A v^3 A C_H}{Q_{ab}} = -\frac{1}{2}\sigma_{ab} C_d \rho_A A v^3 \tag{3}$$

$$\Delta t = \frac{\Delta h}{v\sin\theta} \tag{4}$$

$$g = g_0\left(\frac{R_E}{R_E + h}\right)^2;\ g_0 = -9.81\ m\cdot s^{-2} \tag{5}$$

In these equations, $\theta$ is the angle relative to horizontal, $C_d$ is the drag coefficient[1], $A$ is the instantaneous cross-sectional area, $\rho_A$ is the atmospheric density, $g$ is the gravitational acceleration, $R_E$ is the average radius of the Earth (6.371 x $10^6$ m), $h$ is the instantaneous altitude, and $\sigma_{ab}$ is the ablation coefficient. In Eq. (3), the product of the ablation coefficient, $\sigma_{ab}$, and the drag coefficient, $C_d$, replaces the ratio of the heat transfer coefficient ($C_H$) to the effective heat of ablation ($Q_{ab}$). In the absence of shape-dependent ablation and drag physics, constant values of $\sigma_{ab} = 10^{-8}\ s^2\cdot m^{-2}$ [9] and $C_d = 1.0$ are used.

Equations (1-3) are used to update the velocity, flight path angle, and mass at each altitude step, which is usually set to 10 m increments. The cross-sectional area, $A$, is also reduced based on the decreased mass, assuming constant, uniform density and spherical shape. For each iteration, the atmospheric density is interpolated from the 1976 standard atmosphere tables, and the gravitational acceleration is computed from Eq. (5). The derivatives are then recomputed and the

[1] The engineering convention is used for the drag coefficient in this paper, where drag is $\frac{1}{2}C_d A\rho_A v^2$. The factor of ½ is often omitted in the literature, so the $C_d$ values may differ by a factor of two from the references.

process repeats until the bolide reaches the ground or the flow conditions reach the specified breakup criterion. Once fragmentation begins, flight integration is computed similarly for the resulting fragments and/or pancaking clouds, as described below for each model.

## *2.2 Breakup Criteria*

Following [2, 7, 11], a breakup event is assumed to occur when the pressure, $P$, at the leading edge stagnation point of the bolide exceeds a specified breakup threshold, $S$, as defined by Eq. (8). Although this parameter is broadly referred to as "strength" for convenience, it does not represent a specific material property of the bolide, such as yield strength, compressive strength, or tensile strength. Rather, it acts as a generalized proxy for bulk/aggregate strength by representing the flight conditions under which the body is assumed to fail.

$$(P = \rho_A v^2) \geq S \tag{8}$$

For models that allow multiple discrete fragmentations, the breakup strengths of the resulting fragments increase according to Eq. (9) [8, 11, 16], where $\alpha$ is an exponential strength scaling parameter, and subscripts $c$ and $p$ refer to the child and parent fragment, respectively.

$$S_c = S_p \left(\frac{m_p}{m_c}\right)^{\alpha} \tag{9}$$

Smaller fragments are assumed to have proportionately larger strength because crack size is assumed to scale with the size (mass) of the object. Larger masses, therefore, have larger cracks and the smaller masses have smaller cracks. Particularly at larger scales, the pre-entry crack structure is assumed to determine the bulk strength of the object. Only when sizes become relatively small does the material strength of the constituent material govern the bulk strength. The maximum strength of the material is set at 330 MPa, in accordance with laboratory compression yield tests of discovered meteorite falls [4]. The strength of a fragment is not permitted to exceed this maximum value. The initial strength of the asteroid when it enters the atmosphere, $S_0$, is an unknown parameter [17] that will be considered in the context of the modeling approaches. Appropriate values for the scaling coefficient, $\alpha$, are chosen empirically [11, 17] or are allowed to vary stochastically throughout the simulation. While values have been suggested for each, a lack of knowledge of the internal structure and pre-fracture patterns of asteroids prior to atmospheric entry forces them to be treated as modeling parameters, with Eqs. (8-9) acting as proxies for the true strength.

## *2.3 Continuous Pancake Fragmentation*

The pancake model (Fig. 1) stems from Hills and Goda [9] and has been widely used in risk modeling [1, 2]. At the initial breakup point, the bolide loses its strength and becomes a cloud of continuously fragmenting material that is modeled as a single deforming body. The cloud begins as a sphere and then begins to spread out and flatten (or "pancake") under a single bow shock, due to pressure differences between the front and sides of the debris cloud. The lateral spread

rate is computed based on a dispersion velocity proportional to the square root of the air-to-bolide density ratio and the instantaneous velocity [9, 18]:

$$v_{disp} = \left(\frac{7}{2}\frac{\rho_A}{\rho_b}\right)^{\frac{1}{2}} v. \tag{10}$$

The cross-sectional area in Eq. (2-3) is then calculated at the next time step as

$$A = \pi\left(r_{old} + v_{disp} * dt\right)^2. \tag{11}$$

As the fragments on the leading edge spread out, gaps are assumed to be filled in by trailing mass from the ongoing breakup process. The cloud continues to flatten and slow under a common bow shock until the end of flight. This is a deviation from the original Hills and Goda [9] model, which assumes that a common bow shock is only maintained while the radius of the cloud is less than twice that of the initial bolide. Implications of this assumption are discussed further in the light curve comparison section. Flight path integration and mass loss due to ablation continues throughout the process until the cloud fully ablates, slows below a limiting velocity, or reaches the ground.

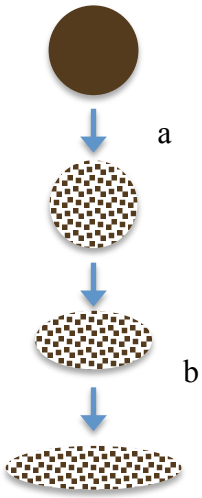


Figure 1: Liquid drop/ pancake model. (a) Breaks into dust cloud. (b) Spreads out and propagates to ground.

## *2.4 Discrete Fragmentation with Collective Wake*

This simplified fragmentation model (Fig. 2), built loosely on the work of ReVelle [5, 6], incorporates multiple fragmentation events and a different method of representing the flight of constituent pieces under a common bow shock. When the bolide breaks, the model assumes two equally sized fragments, each with half the mass of the parent. The two fragments are assumed to then fly next to each other within a common bow shock, such that the total frontal area of the

formation is doubled, presumably either with each fragment maintaining the same area as the parent or with dust filling in any open spaces between smaller-area children. In this way, each fragmentation event halves the formation's ballistic coefficient as seen in Eq. (12), which effectively doubles the drag work and ablation at each break. There are some geometric inconsistencies with this scheme, as spheres consisting of half the original mass will not create the doubling of the drag area. However, this is the construct of the original model and will be followed here.

$$B = \frac{m}{C_d * A_p} \rightarrow B = \frac{m}{C_d * 2A_p} \tag{12}$$

The fragment strengths are assumed to increase according to Eq. (9). Although the mass of the formation remains the same, the strength increases based on the halved mass of its constituent fragments. This allows the strength to scale up with successive breaks, spacing out the fragmentation events, while also preserving the total amount of mass behind the single bow shock. Since air density is exponentially increasing and the deceleration due to drag is small at first, the ram pressure continues to build, fracturing the fragments again. At each successive fragmentation, the frontal area doubles and the strength is further increased. The formation stays within a single bow shock throughout the entire process, continuing to break and expand at each instance that the condition in Eq. (8) is met.

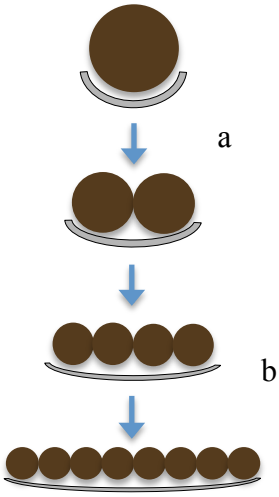


Figure 2: Collective wake model. (a) Breaks and ballistic coefficient halves. (b) Process continues to ground under a single bow shock.

## *2.5 Discrete Fragmentation with Non-collective Wake*

ReVelle [5, 6] also describes a model (Fig. 3) without collective wake behavior. In this model, each fragmentation event produces two equally sized children, as in the collective wake case, but one of the fragments is lost to the wake [5] rather than flying in formation with the other fragment. The surviving fragment maintains the pre-break velocity and cross-sectional area, but

only half of the pre-break mass. Essentially, this causes half of the energy to be quickly lost, or deposited, at each break. As with the collective wake behavior, the ballistic coefficient drops by half at each break (Eq. 13), but in this case it is due to reduction in mass rather than increase in area, and so half of the system's energy is also "lost" in the process. This is fundamentally different than all of the other models in this paper, where the energy loss is physically accounted for through drag and ablation. No specific physical arguments are given in Refs [5,6] to explain the mechanism for the mass loss, but original model is followed here for comparison. In this implementation, the fragment gains strength according to Eq. (9) and continues flight until it breaks again.

$$B = \frac{m}{C * A_p} \rightarrow B = \frac{m/2}{C * A_p} \tag{13}$$

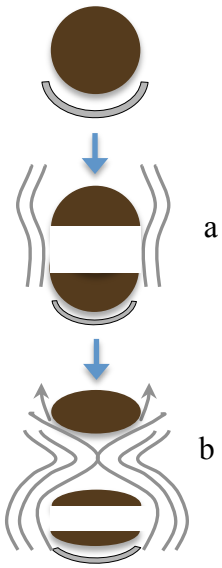


Figure 3: Non-collective wake model.
(a) Breaks and ballistic coefficient halves.
(b) Trailing fragment separates from lead body.

## *2.6 Discrete Fragmentation with Independent Wakes*

Mehta [11] proposed an alternate approach (Fig. 4) for estimating the ground footprint resulting from asteroid breakup. Though energy deposition does not appear explicitly in the work, the approach offers an additional comparison. In this approach, a bolide fragments into two independent spherical bodies. The original paper varies the mass split ration stochastically, but in the current implementation a 50/50 split has been assumed to compare with the other models. The children are assigned new strengths defined by Eq. (9), and each is considered to be independent, with a separate bow shock, immediately after the fragmentation event. While the fragments would require an imparted lateral velocity to separate such that they do not interact with any other fragments, this lateral velocity is assumed small compared to the total velocity

and the fragments begin with the same trajectory as the parent. As the ram pressure continues to increase with descent into thicker atmosphere, the children are permitted to fragment accordingly, resulting in continually smaller and stronger bolides. In this case, each child has half the pre-break mass but only 63% ( $½^{2/3}$) of the associated drag area, which decreases the ballistic coefficient by approximately 20%. The independent wake assumptions means that each break increases the energy deposition less compared to the other models.

$$B = \frac{m}{C*A_p} \rightarrow B = \frac{m/2}{C*0.63A_p} \rightarrow B \approx 0.8\frac{m}{C*A_p} \tag{14}$$

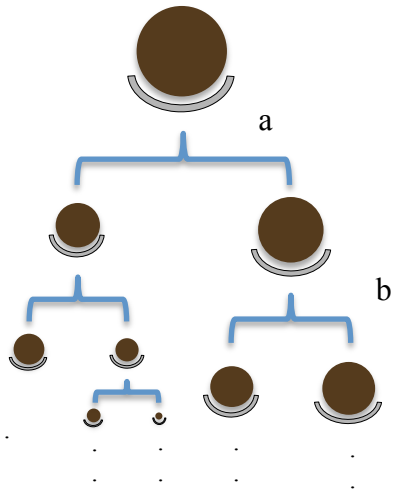


Figure 4: Independent wake model.
(a) Breaks into two discrete fragments with independent bow shocks.
(b) Process continues to ground.

## *2.7 Combination Fragmentation Model*

The final model presented here (Fig. 5) unites elements of the pancake and discrete fragment models to create a more comprehensive and intuitive representation of the breakup process. While the idea has been touched on previously [13], the model is defined specifically here. When a bolide breaks, three objects result: two spherical fragments and a dust cloud. The fragments sizes are determined by separating the parent bolide into two parts such that $r_{child,1} + r_{child,2} = r_{parent}$. It is assumed that the children originate without distinct shapes, but immediately become spheres in which any asymmetries are sheared off by pressure and group together to form the dust cloud. The mass of each independent fragment is then computed from its new radius and the

constant, uniform bolide density. The remaining material, after subtracting the child fragment masses from the parent mass, forms a dust cloud.

The radius-based split approach was selected so that the radius split ratio could be used as a single parameter to control the mass of each discrete fragment as well as the mass of the cloud. The radius split fraction is taken to be between 1% and 50% of the parent radius (leaving 50% to 99% of the parent radius to the sibling fragment), corresponding to potential dust cloud masses between 3% and 75% of the parent mass. The maximum cloud mass occurs when the fragments are equally sized, and 77% of all possible splits result in a dust cloud with greater than half of the parent mass. The split ratio can be varied stochastically, fixed, or specified for each break.

The dust cloud created at each break is taken to behave according to the pancake model presented above. Instead of one single cloud representing the overall breakup behavior, smaller clouds produced in each fragmentation event can more specifically represent the fractional amount of dust and debris that may blow off at different points and deposit energy at different rates. Each cloud is initialized as a sphere of the same density, velocity, and flight path angle as the parent bolide, and then immediately begins to spread. Each cloud continues to descend and spread until it reaches the ground or ablates to negligible mass.

The discrete fragments and dust clouds that are produced are all considered independently from each other. Similarly to the independent wake model, the fragments are assumed to have separate bow shocks immediately upon formation and begin on the pre-break trajectory. Each fragment attains an increased strength by Eq. (9), and each is allowed to fragment further once the breaking condition in Eq. (8) is met. In subsequent fragmentations, an identical process is carried out, with the formation of another flattening dust cloud and two distinct children.

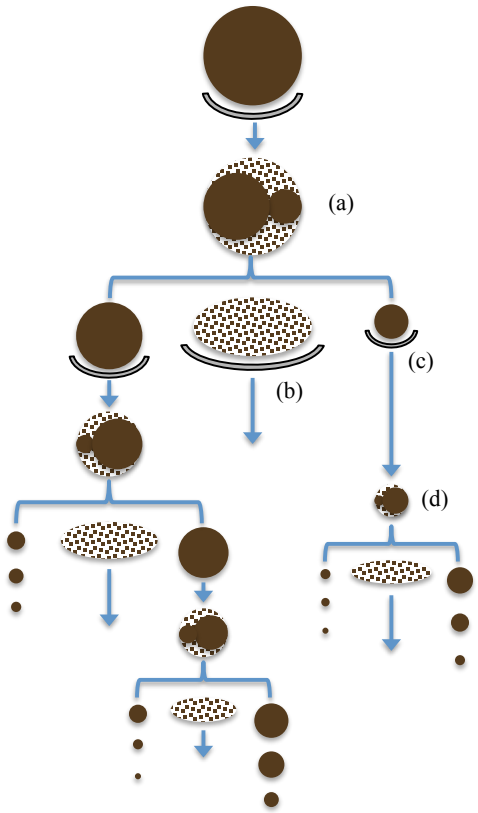


Figure 5: Combination model. (a) Breaks into two fragments and a dust cloud. (b) Dust cloud pancakes. (c) New fragments begin independent propagation. (d) Process continues as described.

## *2.8 Energy Deposition*

The atmospheric energy deposition is approximated as the system's total change in kinetic energy per unit altitude. All of the kinetic energy lost through the mass and velocity changes of Eqs. (1) and (3) is assumed to be deposited within the given altitude increment. The kinetic energy of each fragment and/or cloud produced during breakup is computed at each altitude, and the energy deposition is computed as the change in energy divided by the change in altitude:

$$E_{dep}(h) = \frac{dE}{dh} = \frac{1}{2}\left(\frac{m_2 v_2^2 - m_1 v_1^2}{h_2 - h_1}\right) \tag{15}$$

The total energy deposition is the sum of the energy deposited by all clouds and fragments at each altitude, converted to units of kilotons per kilometer. As mentioned, a constant altitude increment is used for the flight integration and energy deposition. For multi-body models, this approach neglects potential differences in the times at which the individual pieces may pass

through a given altitude, and assumes that those differences are small enough to be insignificant. The cases run for this study used 10 m altitude increments, which provides sufficient spatial resolution and results in increments that keep the explicit time integration scheme well-behaved.

## 3.0 Chelyabinsk Breakup Comparison

In February 2013, a 20-meter diameter asteroid entered the Earth's atmosphere and airburst at approximately 30 kilometers over Chelyabinsk, Russia. There is significant documentation and data from this event [4], including reproductions of the asteroid's light curve [14], from which the energy deposited into the atmosphere as the bolide fragments and ablates can be inferred. Replicating the resulting energy deposition curve offers clues to physical processes that may occur in similar events. In addition, comparing assumptions and results across the current models allows for a more comprehensive understanding of the entry modeling process. Results provide insight into the values of uncertain modeling parameters, such as the initial strength and strength scaling coefficient, that are appropriate for this event.

In this study, each of the five models described above was used to qualitatively match the energy deposition derived by Brown et al. [14] by varying the available fragmentation parameters. For the pancake model, initial breakup strength, $S_0$, is the only fragmentation variable, though effects of limiting the maximum radius of the cloud are also considered. For the three discrete fragmentation models, initial breakup strength and the strength scaling parameter $\alpha$ can both be varied. For the combination model, the split fraction defining the relative fragment sizes and cloud masses provides a third independent parameter in addition to the strength parameters. While different split fractions could be prescribed at each break to match the light curve more explicitly, a single specific split ratio was chosen a priori for this comparison in an effort to maintain consistency across the models. Combination model cases were run both with an even (50/50) split for comparison with the other discrete model results, and with different combinations of fixed split ratio and alpha to better match the actual event. For all cases, the asteroid is assumed to have a diameter of 19.8 m, velocity of 19.16 km/s, entry angle of 18.3°, and density of 3.3 g/cm$^3$ [4] at an initial entry point of 100 km altitude. Note that the entry parameters adopted from [4] give a total initial impact energy of 588 kilotons, while the total energy represented in the Brown curve is only 463 kilotons. Consequently, the model results intrinsically represent ~27% more energy, either deposited or carried to ground, than the observational data.

Table 1 lists the parameters used to best approximate the Chelyabinsk data for each model, and Figs. 6-7 show the comparisons the resulting energy deposition curves. The results and implications from each comparison are discussed in the following subsections. The primary features considered in the qualitative matching and comparisons are the peak energy deposition, altitude, width, and overall shape. Each curve in Figs. 6-7 is shown at two plot resolutions: a 10-m altitude resolution showing every altitude step computed, and a 1-km resolution in which the 10-m results have been averaged over each kilometer of altitude. The finer resolution enables the

more detailed model behaviors to be compared, while the averaged results are closer to the resolution of the observational data, provide a better picture of the overall energy deposition trends, and may be more representative of how the more detailed processes may actually appear as an observed light curve.

Attempting to match the shape of the curve highlights the differences between the physical assumptions of the models. The Chelyabinsk bolide deposited most of its energy between 40 km and 20 km altitude with similar energy deposition rates above and below the peak. This roughly symmetrical shape, along with the additional fragmentation that occurred a few kilometers lower, challenges the capabilities of the models.

Table 1: Parameters used to match the Chelyabinsk energy deposition curve for each model.

| | Pancake | Collective Wake | Non-Collective Wake | Independent Wake | Combination | |
|---|---|---|---|---|---|---|
| $\sigma_0$ (MPa) | 1.6 | 1.55 | 1.6 | 1.55 | 1.55 | 1.55 |
| α | n/a | 0.3 | 0.5 | 0.1 | 0.1 | 0.57 |
| Split fraction | n/a | 50/50 mass | 50/50 mass | 50/50 mass | 50/50 radius | 60/40 radius |

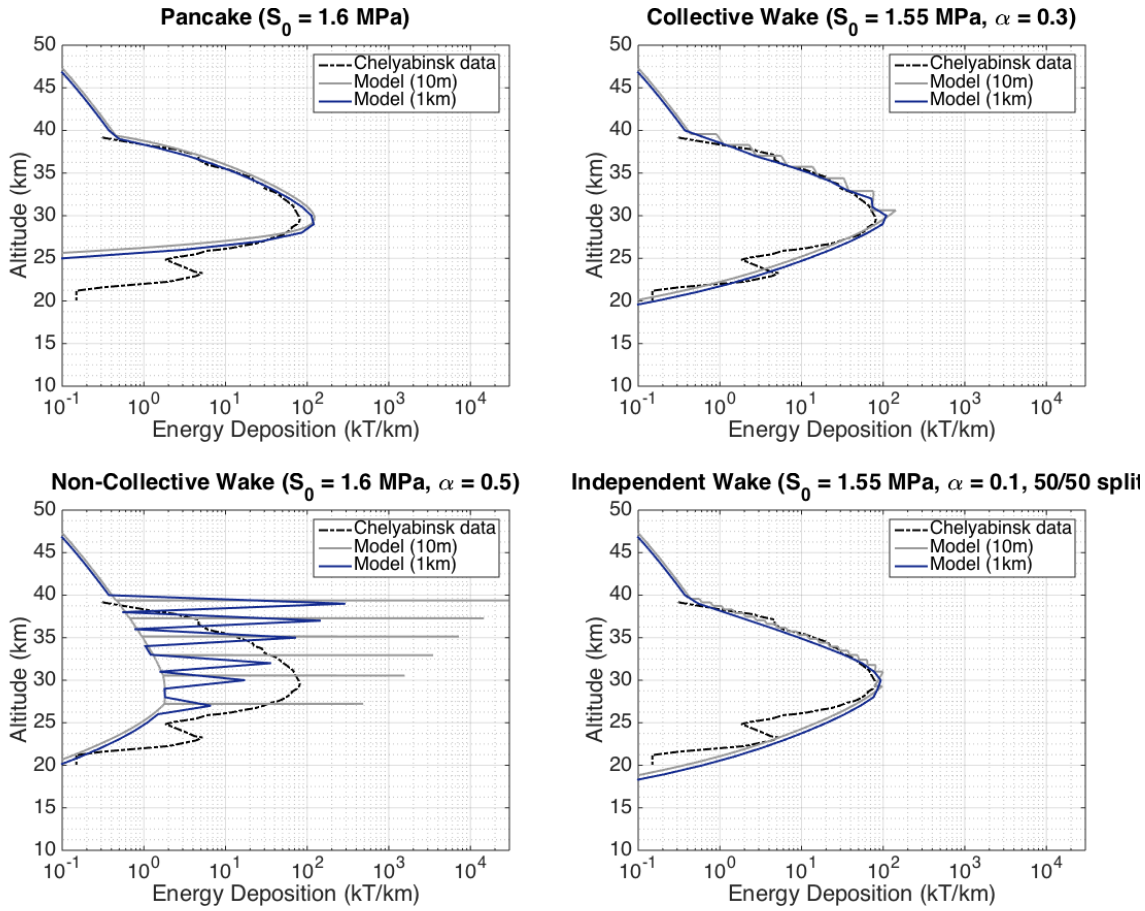


Figure 6. Energy deposition curve from the pancake model and three discrete fragmentation models, matched to Chelyabinsk observational data with the parameters listed in Table 1.

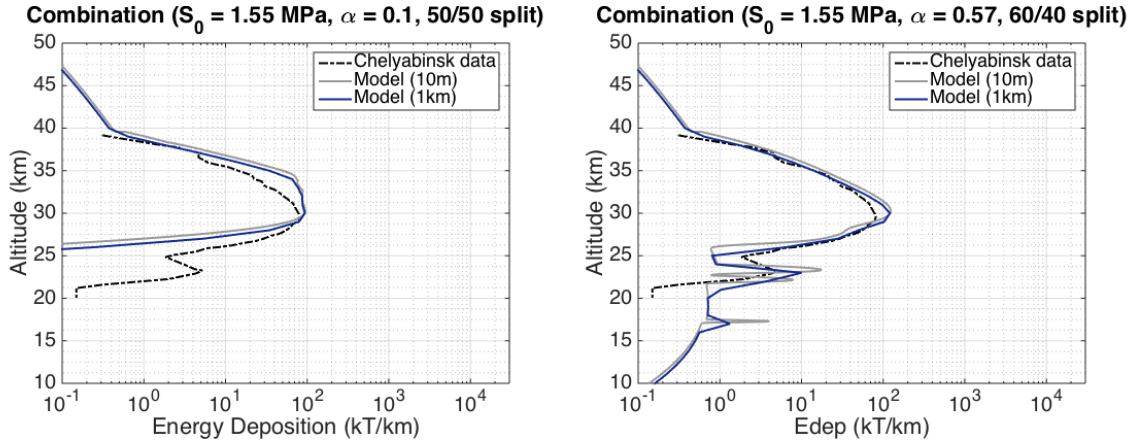


Figure 7. Energy deposition curve from the combination model, matched to Chelyabinsk observational data with the parameters listed in Table 1.

### *3.1 Pancake Model Results*

The overall profile shape, width, and altitudes match very closely, although the predicted peak exceeds the measured value by around 50%. Only the primary peak is represented since the pancake model does not permit the multiple breaks that would be associated with the smaller flare seen at around 22 km altitude. The good match in the altitudes of both the initial break and peak energy deposition suggests that the majority this asteroid's energy deposition can be well represented with a dust cloud like analogy.

The Hills and Goda [9] presentation of this approach mentions that the pancake analogy only holds up to a radius increase of 2 times the initial bolide radius, after which the pieces would not maintain a common bow shock. The model implemented here, however, allows the cloud to continue spreading beyond this limit while still assuming a common bow shock. This may contribute to the model's tendency to exceed the observed peak energy deposition. To investigate the effects of this assumption/, different cloud radius limits were imposed on the Chelyabinsk comparison case.

Fig. 8 shows results for the same parameters as in the Chelyabinsk comparison case, with limits of 2, 7, and 10 times the initial radius. Limiting the cloud spread to twice the initial radius increases the width of the energy deposition peak, lowers the peak altitude, and lowers the peak magnitude so that it no longer represents the observed results. Limiting the radius to seven times the original size restores a general match, reduces the peak maximum to a closer match with the observed data, and encompasses the secondary peak within the main profile rather than matching the width of the primary peak. Capping the cloud at 10 times the original radius (which the cloud reaches right around the peak energy deposition point at 30 km altitude) very nearly reproduces the results in Fig. 6a, suggesting that cloud growth beyond a factor of 10 has little impact on the energy deposition. The unconstrained case ultimately grows to 65 times the initial radius before hitting the ground. While there is likely a size limit at which the individual fragments can no longer be represented by a cloud analogy, the current results suggest this limit is closer to 10 than 2.

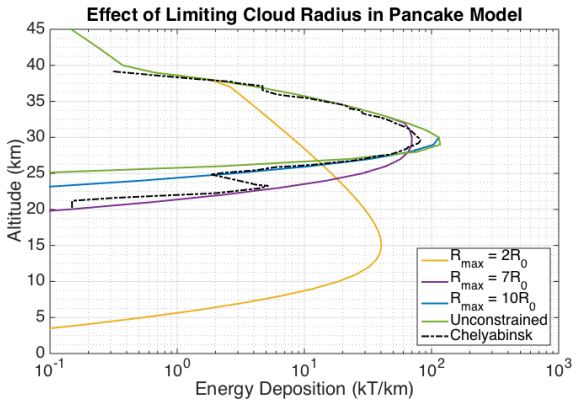


Figure 8: Effects of cloud radius limits ($R_{max}$) on pancake model results for Chelyabinsk meteor energy deposition.

## *3.2 Collective Wake Model Results*

The collective wake model also deposits energy through the increasing frontal area, but does so through successive, discrete fragmentations. Instead of being controlled by a dispersion velocity, the shape of the profile is controlled by the fragmentation rate dictated by the strength scaling of each fragment generation.

The collective wake model's peak energy deposition altitude and general curve shape match the observed results well. A notable difference is the stair-step behavior that corresponds to each fragmentation event. As the frontal area of the formation increases with each successive break, there is a discontinuity in the rate of energy deposition. The original ReVelle model includes a time delay term that phases in the area growth over a user-specified duration. This term was left out because it is an arbitrary smoothing function and does not directly change the magnitude of the energy deposition rate. As with the pancake model, the peak energy deposition rate exceeds the observed value by around 34-75% (at 1-km and 10-m resolutions, respectively). The bottom portion of the curve more closely represents the shape observed, but this model also fails to represent the secondary peak.

## *3.3 Non-collective Wake Model Results*

Because this approach retains a constant frontal area but loses half of the mass during each successive fragmentation, the energy deposition behavior is driven by mass loss rather than by deceleration. Because significant mass is lost instantaneously during each fragmentation, most of the energy is deposited as large, distinct spikes. Also, since the model assumes even fragment sizes with 50% of the mass lost at each break, the first break corresponds with the largest deposition, the second break the second largest, and so on. Again, since there is no frontal area increase, once the mass is lost to the wake, the energy deposition curve reverts to the value just before the break point. It becomes apparent that such a model does not represent a Chelyabinsk like event.

### *3.4 Independent Wake Model Results*

In the current implementation, the fragments split into two even, independent spheres and the total frontal area increases by a factor of only ~1.26 (2 fragments each with area $A_c=0.63A_p$) with each break, rather than the factor of two or more seen in the pancake and collective wake models. As a result, the fragmentation process must occur much more frequently to represent the light curve. This is achieved through a lower strength scaling parameter value, $\alpha = 0.1$ in this case, which allows a more continuous breakup process. The plot illustrates this through the finer stair-steps along the upper portion of the curve. By comparison, the collective wake model is able to reasonably match the light curve with 128 fragments in seven breaks, while the independent wake model requires nearly 1 million fragments to generate the result in Fig. 10. Overall, the match to the observed curve is quite good, and the peak energy deposition rate is within 15-22% of the observed value. But, again, the model is unable to capture a secondary peak.

### *3.5 Combination Model Results*

As discussed earlier, the combination model provides additional fragmentation control through the split ratio of the discrete fragments and the corresponding amount of mass introduced as a cloud. For the initial Chelyabinsk modeling comparisons, fixed split ratios were applied to all fragmentations within a run.

Figure 7a shows the energy deposition results using the combination model with the same initial breakup strength (1.55 MPa) and strength scaling parameter ($\alpha = 0.1$) used for the independent wake results. An even 50/50 radius split was used to most closely match the even mass-split assumption of previous results, though the radius-split fragments are each only 12.5% of the parent mass, with the remaining 75% going to a cloud. While the initial break altitude and peak energy deposition rate are close matches to the Chelyabinsk data (within 15-17%), the nose of the peak has widened and too much energy is deposited prior to 30km. This is a result of effectively double-representing the cloud behavior by both explicitly including a cloud and attempting to mimic cloud-like behavior with the low strength gain and rapid breaking for the discrete fragments.

To match the combination model to the Chelyabinsk curve, larger strength scaling values and un-even split ratios were applied. Increasing the strength scaling parameter increases the strength gain at each break, delaying the subsequent breaks and associated energy deposition. Figure 7b, shows the results obtained with $\alpha = 0.57$ and a 60/40% radius split. Not only has the peak width narrowed, but a secondary peak has emerged. The magnitude of the peak in Fig. 7b exceeds that in Fig. 7a as the additional energy is carried lower by stronger fragments, and is around 50% larger than the Chelyabinsk peak.

Because the split fraction is applied to the radius, the pancaking dust clouds are usually formed from a significant portion of the parent mass. Fig. 9 shows the relative energy deposition contributions of the clouds and fragments for the case shown in Fig. 7b. The fragments contribute a few orders of magnitude less energy than the dust cloud throughout much of the asteroid's flight. Once the bolide is finished fragmenting, no further dust clouds are produced, and the total energy deposition curve follows the fragments' curve. Including additional fragmentations produces spikes in the curve at low altitudes.

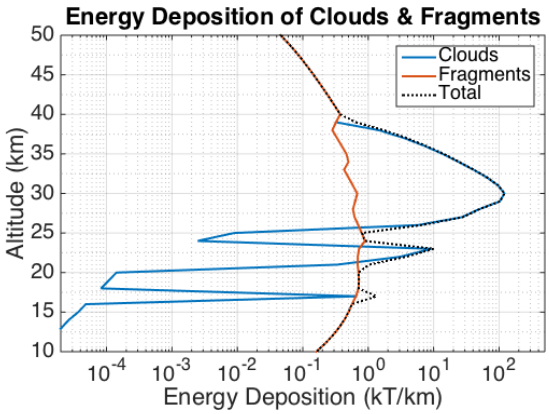


Figure 9: Contributions to energy deposition of the dust clouds and discrete fragments in the combination model. After initial fragmentation, the dust cloud dominates energy deposition, but later in flight the total is due mainly to the persisting fragments.

The combination of discrete fragments and multiple pancaking dust clouds enables better reproduction of the measured results, and permits more inference about the actual Chelyabinsk event through the variation of additional modeling parameters. The combination model results highlight that, for an event like Chelyabinsk, the energy deposition is related to cloud-like breakup behavior. In fact, even the discrete fragment models are only able to represent the observations when run in a way that emulates cloud-like energy deposition. However, the ability to represent more than a single flare requires that multiple bursts be permitted. In the combination model, this is done through the persistence of stronger discrete fragments. These fragments then subsequently breakup, releasing a flare-producing cloud at a lower altitude.

### *3.6 Split Fraction and Strength Scaling Variations in the Combination Model*

Figure 10 shows a comparison of the combination model results for the Chelyabinsk case with different fixed split fractions and alpha values. As described above, a 50/50 split fraction generates the largest mass of dust, reducing the total number of fragmentations and peaks. Constant 95/5 split fractions produce more distinct peaks as little pieces continually slough off the parent rock. Secondly, specifying only 95/5 splits generates a peak of lesser width at an altitude closer to the initial break height. Because the larger fragment involved in this splitting regime is similar in mass to the parent body, its strength increases only slightly with each

fragmentation. This allows it to continue breaking many times within a small distance in an event that can be likened to an airburst. Moreover, the whole fragmentation process happens more smoothly for 95/5 splits than for 50/50 splits, such that fragmentations are less apparent once the majority of the initial energy has already been deposited.

Variations in the strength gain exponent also contribute to the width and altitude of the peak. Simulations with primarily low α values have narrower peaks at higher altitudes, whereas larger α values generate wider and lower peaks. Stronger fragments persist farther before fragmenting and therefore deposit their energy lower in the atmosphere.

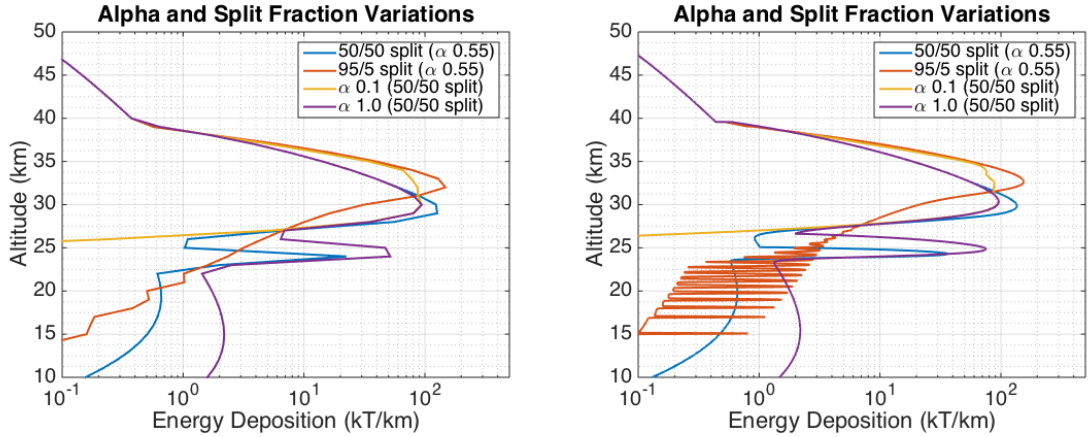


Figure 10: Effects of different radius split fractions and α values in the combination model, for the Chelyabinsk case with an initial breakup strength of 1.55 MPa (plotted at 1-km resolution on the left and 10-m resolution on the right).

## *3.7 Stochastic Fragmentation*

Of course, an actual event is not governed by fixed split ratios as has been assumed in the preceding cases. Although no modeling effort is capable of capturing the exact pattern of cracks and the sizes of fragments as they break off from a parent body, allowing a distribution across many possible split fractions and strength gain exponents produces a range of possible results that will span actual events. Figure 11 displays 500 simulations of the Chelyabinsk entry using the combination model with the strength scaling and radius split fractions allowed to vary stochastically with each fragmentation event. The Chelyabinsk entry parameters and an initial strength of 1.55 MPa are held constant between the cases so that the only variable in the process is the randomness involved in fragmentation. Each break occurs with a split fraction between 50/50 and 95/5, and a strength scaling parameter between 0.1-1 is used to increase the strength of both resulting fragments according to their relative size (i.e., both fragments in a given break take the same α value, but have different final strengths due to their relative sizes). The energy deposition curves from these runs are overlaid and grayed out to form a swath of viable curves. The Chelyabinsk light curve is plotted on top for reference, and appears within the bounds of the stochastic band.

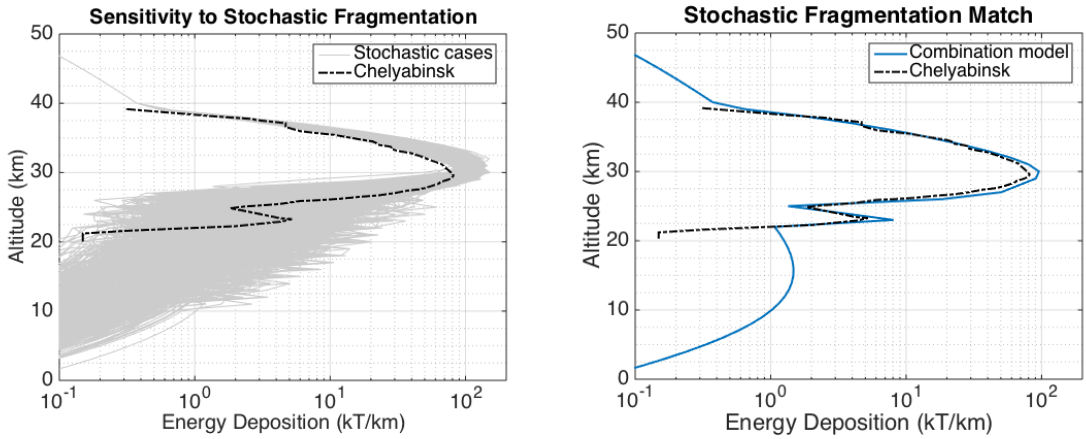


Figure 11: Range of combination model results (left) and a sample curve-matched case (right) from 500 simulations of the Chelyabinsk entry case with strength scaling and radius split parameters varied stochastically at each fragmentation event: $\sigma_0$ = 1.55 MPa, $\alpha$ = 0.1-1.0, split fraction = 50/50-95/5 radius.

An important result is that, although the randomness in the split behavior does greatly affect the curve features below the peak, the actual peak deposition rate and altitude are not drastically changed. This shows some robustness to the randomness in the model and implies that detailed knowledge of the internal structure may not be required to generate reasonable energy deposition curves.

In addition to considering the range of results as a whole, the individual samples in the Monte Carlo assessment can be queried to find the closest match. The right plot in Figure 11 shows an example case extracted from the results in the plot on the left. The combination model effectively matches the peak altitude and magnitude of the observed light curve, overestimating the first peak by about 15-20%. It can also produce a second peak corresponding to the fragmentation event around 22 km altitude, though the predicted magnitude is 50-60% larger than expected. Reproducing a single secondary peak, rather than many smaller subsequent peaks, was most readily accomplished using a relatively small number of break events (limited by high strength gains). This, however, also results in larger fragments continuing to deposit more energy well below the main peak, which appears as the hump at the bottom of the curve. The initial strength was set to accurately reproduce the peak altitude, and the upper curve slope suggests the energy deposition is initially dominated by the first dust cloud.

# Conclusion

Simple models of asteroid fragmentation and corresponding energy deposition were compared for application to impact risk assessment. Four models from the existing literature, one pancake model and three discrete fragment models, were used to model the Chelyabinsk meteor, as was a fifth model created by combining pieces of the former models. All of the models, excepting the non-collective wake discrete fragment approach, were able to match the main energy deposition

curve derived from the Chelyabinsk light curve. All of the discrete fragment models that were able to match the data required inputs that forced the discrete fragment production to mimic a cloud-like behavior. This implies that the energy deposition for large flare events, such as witnessed in Chelyabinsk, is driven by clouds of dust or small fragments that behave in an analogous, aggregate fashion. The newly presented combination model was able to reproduce the observed peak, and was also able to represent a smaller post-breakup flare. A Monte Carlo simulation of the event was performed using the combination model, allowing the mass split and strength gain to vary stochastically at each break event. The main energy deposition peak and location was fairly constant throughout the simulation, but the post breakup results varied widely. For applications concerned with the primary flare, these results suggest that cloud-like behavior is necessary, but a detailed description of the object may not be required. Subsequent flares however, appear to be strongly dependent on the specific breakup characteristics.

## Acknowledgements

The authors would like to thank the Asteroid Threat Assessment Project (ATAP) at NASA Ames Research Center, under which this work was performed, and the ATAP funding manager, Lindley Johnson, at NASA's Planetary Defense Coordination Office. The authors would also like to thank Jessie Dotson, David Morrison, and Michael Aftosmis of NASA Ames for their reviews and insight in preparing this manuscript.

## References

1. Motiwala, S. A., Mathias, D. L., and Mattenberger, C. J., "An Integrated Physics-based Risk Model for Assessing the Asteroid Threat," *International Topical Meeting on Probabilistic Safety Assessment and Analysis*, Sun Valley, ID, pp. 26-30 April 2015.
2. Stokes et al., "Study to Determine the Feasibility of Extending the Search for Near-Earth Objects to Smaller Limiting Diameters," *National Aeronautics and Space Administration*, 2003.
3. Toon, O. B., Zahnle, K., Morrison, D., Turco, R. P., and Covey, "Environmental Perturbations Caused by the Impacts of Asteroids and Comets," *Reviews of Geophysics* (35-1), pp. 41-78, 1997.
4. Popova, O. P., Jenniskens, P., Emel'yanenko, V., et al., "Chelyabinsk Airburst, Damage Assessment, Meteorite Recovery, and Characterization," *Science* (342), p. 1069, 2013.
5. Revelle, D. O., "NEO fireball diversity: energetics-based entry modeling and analysis techniques," *Near Earth Objects, our Celestial Neighbors: Opportunity and Risk, Proceedings IAU Symposium* (236), pp. 95-106, 2007.
6. Revelle, D. O., "Recent Advances in Bolide Entry Modeling: A Bolide Potpourri," *Earth, Moon, and Planets* (95), pp. 441-476, 2005.
7. Bland, P. A. and Artemieva, N. A., "The rate of small impacts on Earth," *Meteoritics & Planetary Science* (41-4), pp. 607-631, 2006.

8. Artemieva, N. A. and Shuvalov, V. V., "Motion of a fragmented meteoroid through the planetary atmosphere," *Journal of Geophysical Research* (106-E2), pp. 3297-3309, 2001.
9. Hills, J. G., Goda M. P., "The Fragmentation of Small Asteroids in the Atmosphere," *The Astronomical Journal* (105-3), pp. 1114-1144, 1993.
10. Chyba, C. F., Thomas, P. J., and Zahnle, K. J., "The 1908 Tunguska explosion; atmospheric disruption of a stony asteroid," *Nature* (301), pp. 40-44, 1993.
11. Mehta, P. M., Minisci, E. M., Vasile, M., "Break-up Modelling and Trajectory Simulation Under Uncertainty for Asteroids," *4th IAA PDC*, Rome, Italy, 2015.
12. Artemieva, N. A. and Shuvalov, V. V., "Interaction of shock waves during the passage of disrupted meteoroid through atmosphere," *Shock Waves* (5-6), pp. 359-367, 1996.
13. Popova, O., "Passage of Bolides through the Atmosphere," *Meteoroids: The Smallest Solar System Bodies*," pp. 232-242, 2011.
14. Brown, P. G., et al., "A 500-kiloton airburst over Chelyabinsk and an enhanced hazard from small impactors," *Nature* (503-7475), pp. 238-241, 2013.
15. Opik, E. J., Physics of Meteor Flight in the Atmosphere, Interscience, New York, 1958
16. Weibull, W. A., "A statistical distribution function of wide applicability," *J. Applied Mechanics* (10), pp. 140-147, 1951.
17. Popova, O. P., et al., "Very low strengths of interplanetary meteoroids and small asteroids," *Meteoritics & Planetary Science* (46-10), pp. 1525-1550, 2011.
18. Passey, Q. R. and Melosh, H. J., "Effects of Atmospheric Breakup on Crater Field Formation," *Icarus* (42), pp. 211-233, 1980.